Far-field interference of a neutron white beam and the applications to noninvasive phase-contrast imaging

D. A. Pushin,[1,2,*] D. Sarenac,[1,2] D. S. Hussey,[3] H. Miao,[4] M. Arif,[3] D. G. Cory,[2,5,6,7] M. G. Huber,[3] D. L. Jacobson,[3] J. M. LaManna,[3] J. D. Parker,[8] T. Shinohara,[9] W. Ueno,[9] and H. Wen[4]

[1]*Department of Physics, University of Waterloo, Waterloo, Ontario, Canada N2L3G1*

[2]*Institute for Quantum Computing, University of Waterloo, Waterloo, Ontario, Canada N2L3G1*

[3]*National Institute of Standards and Technology, Gaithersburg, Maryland 20899, USA*

[4]*Biophysics and Biochemistry Center, National Heart, Lung and Blood Institute, National Institutes of Health, Bethesda, Maryland 20892, USA*

[5]*Department of Chemistry, University of Waterloo, Waterloo, Ontario, Canada N2L3G1*

[6]*Perimeter Institute for Theoretical Physics, Waterloo, Ontario, Canada N2L2Y5*

[7]*Canadian Institute for Advanced Research, Toronto, Ontario, Canada M5G 1Z8*

[8]*Research and Development Division, Neutron Science and Technology Center, Comprehensive Research Organization for Science and Society (CROSS), 162-1 Shirakata, Tokai, Ibaraki 319-1106, Japan*

[9]*Materials and Life Science Division, J-PARC Center Japan Atomic Energy Agency (JAEA), 2-4 Shirakata, Tokai, Ibaraki 319-1195, Japan*

(Received 19 September 2016; revised manuscript received 13 December 2016; published 26 April 2017)

The phenomenon of interference plays a crucial role in the field of precision measurement science. Wave-particle duality has expanded the well-known interference effects of electromagnetic waves to massive particles. The majority of the wave-particle interference experiments require a near monochromatic beam which limits its applications due to the resulting low intensity. Here we demonstrate white beam interference in the far-field regime using a two-phase-grating neutron interferometer and its application to phase-contrast imaging. The functionality of this interferometer is based on the universal moiré effect that allows us to improve upon the standard Lau setup. Interference fringes were observed with monochromatic and polychromatic neutron beams for both continuous and pulsed beams. Far-field neutron interferometry allows for the full utilization of intense neutron sources for precision measurements of gradient fields. It also overcomes the alignment, stability, and fabrication challenges associated with the more familiar perfect-crystal neutron interferometer, as well as avoids the loss of intensity due to the absorption analyzer grating requirement in Talbot-Lau interferometer.

DOI: 10.1103/PhysRevA.95.043637

I. INTRODUCTION

The discovery of the neutron [1] led to the construction of a variety of phase-sensitive neutron interferometers. Thermal and cold neutrons are a particularly convenient probe of matter and quantum mechanics postulates given their relatively large mass, nanometer-sized wavelengths, and zero electric charge. One of the first neutron interferometers [2] was based on wave-front division using a Fresnel biprism setup. The perfect-crystal neutron interferometer (NI), based on amplitude division, has achieved the most success due to its size and modest path separation of a few centimeters. Numerous perfect-crystal NI experiments have been performed exploring the nature of the neutron and its interactions [3–9]. However, perfect-crystal neutron interferometry requires extreme forms of environmental isolation [10,11], which significantly limits its expansion and development.

Advances in micro- and nanofabrication of periodic structures with features ranging between 1 and 100 μm makes it possible to employ absorption and phase gratings as practical optical components for neutron beams. The first demonstration of a Mach-Zehnder-based grating NI in 1985 [12] used 21-μm periodic reflection gratings as beam splitters for monochromatic ($\lambda = 0.315$ nm) neutrons. A few years later, a three-transmission-phase-grating Mach-Zehnder NI was demonstrated for cold neutrons ($0.2\ \text{nm} < \lambda < 50\ \text{nm}$) [13–16]. The need for cold or very cold neutrons with a high degree of collimation limits the use of such interferometers in material science and condensed-matter research. An alternative approach was the Talbot-Lau interferometer (TLI) proposed by Clauser and Li for cold potassium ions and x-ray interferometry [17] and implemented by Pfeiffer *et al.* for neutrons [18]. The TLI is based on the near-field Talbot effect [19] and uses a combination of absorption and phase gratings. In this setup the sample, introduced in front of the phase grating (middle grating), modifies the phase and amplitude of the Talbot self-image. While the previously mentioned Mach-Zehnder-type grating interferometers are sensitive to phase shifts induced by a sample located in one arm of the interferometer, this near-field TLI is sensitive to phase gradients caused by a sample. Even though chromatic sensitivity of the TLI is reduced, thus leading to a gain in neutron intensity, in this setup the absorption gratings are challenging to manufacture and limits the incident flux reaching the detector; while the neutron wavelength spread will cause contrast loss as the distance to interference fringes (fractional Talbot distance) is inversely proportional to the neutron wavelength.

It has been previously demonstrated for atoms and electromagnetic waves that the two-grating TLI setup produces fringes in the far field [20–23]. This "Lau effect" [24] requires

*dmitry.pushin@uwaterloo.ca

the first grating to be an intensity mask which serves as an array of mutually incoherent sources, and the second grating is either an intensity or a phase mask which through Fresnel diffraction results in the interference pattern on the screen. When the distance between the two gratings is at multiples of half Talbot length, an image of the first grating is produced at the plane at the second grating, and that image beats with the second grating to produce the beat pattern in the far field downstream.

Here we implement a far-field regime interferometer and report the first demonstration of a multibeam, broadband NI using exclusively phase gratings. Both Lau and Talbot effects turned out to be special cases of a more universal moiré effect [25]. The conceptual step forward of our neutron interferometer is to go to the other end of the moiré effect spectrum for the matter waves, where two pure phase masks produce a beat pattern when both the source and the detector are in the far-field range. This interference would be observed even if the two phase gratings are in contact, provided that their periods are appropriately different. The demonstration includes the use of a continuous monochromatic beam ($\lambda = 0.44$ nm), a continuous bichromatic beam (1/3 intensity $\lambda_1 = 0.22$ nm and 2/3 intensity $\lambda_2 = 0.44$ nm), a continuous polychromatic beam (approximately given by a Maxwell-Boltzmann distribution with $T_c = 40$ K or $\lambda_c = 0.5$ nm), and a pulsed neutron beam ($\lambda = 0.5$ nm to $\lambda = 3.5$ nm). The advantages of this setup include the use of widely available thermal and cold neutron beams, relaxed grating fabrication and alignment requirements, and broad wavelength acceptance.

II. TWO-PHASE-GRATING INTERFEROMETER

As the neutron can be described as a matter wave with a de Broglie wavelength $\lambda = 2\pi\hbar/(m_n v_n)$, where $\hbar$ is the reduced Planck's constant, m_n is the neutron mass, and v_n is the neutron velocity, the problem could be treated similar to the x-ray case. The full mathematical treatment of the general situation of a polychromatic beam passing through a double-phase-grating setup (see Fig. 1) is described by Miao *et al.* [25]. Here we give a brief description and the key points of the universal moiré effect in a far-field regime for neutrons.

The experimental setup, shown in Fig. 1, consists of a slit, two identical linear phase gratings of silicon combs with a period of $P_{G_1} = P_{G_2} = 2.4$ μm, and a neutron imaging detector (neutron camera). Although $\pi/2$-phase gratings for a specific neutron wavelength give optimal fringe visibility, available to us were five different gratings with various depths. We had used gratings corresponding to 0.27π phase shift at 0.44-nm wavelength for the mono- and bichromatic setups and 0.2π phase shift at 0.5 nm wavelength for the polychromatic setup.

For a majority of this work, a fast neutron produced in a reactor core is first moderated using heavy water to thermal energies and then further cooled using a liquid hydrogen cold source [26] before traversing a neutron guide, the end of which is a slit. After exiting the slit and propagating in free space, the neutron acquires a transverse coherence length of $\ell_c = \lambda\mathscr{L}/s_w$, where s_w is the width of the slit and $\mathscr{L}$ is the distance between the slit and the point of interest.

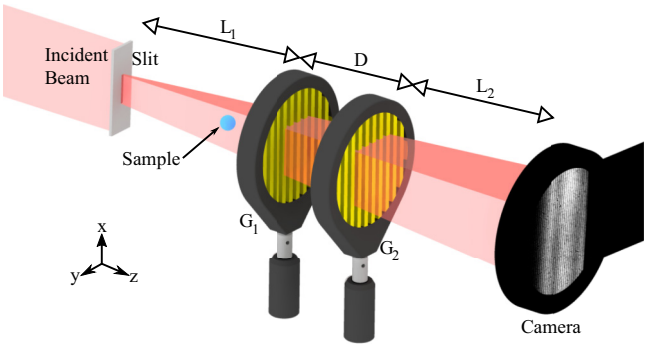

FIG. 1. Schematic of the two-phase-grating interferometer setup. A neutron beam is passed through a narrow slit to define the neutron coherence length along the y direction, which is perpendicular to the grating fringes. Two identical phase gratings (G_1 and G_2) are separated by distance D. They are placed at a distance L_1 from the slit and L_2 from the imaging camera. The fringe pattern at the camera is wavelength *independent* and the fringe visibility can be optimized with the conditions discussed in the text. A sample to be imaged may be placed before the gratings (upstream position) or after the gratings (downstream position).

In order for the neutron to diffract from the first grating G_1 at the distance L_1, the neutron's coherence length (along the y axis in Fig. 1) should be at least equal to the period of the grating:

$$\ell_c = \frac{\lambda L_1}{s_w} \geqslant P_{G_1}. \tag{1}$$

The second grating G_2 is placed at a distance D from the first grating and a distance L_2 from the neutron camera. As neutron cameras have limited spatial resolution η, the fringe period P_d at the camera should be bigger than the neutron camera resolution [25],

$$P_d = \frac{L P_{G_2}}{D} > \eta, \tag{2}$$

where $L = L_1 + D + L_2$ is the distance between the slit and the camera. Similarly, the phase of the fringe pattern on the detector is a periodic function of the slit position, with the period (often called source period) given by [25]

$$P_s = \frac{L P_{G_1}}{D}. \tag{3}$$

Therefore, in order to observe a fringe pattern on the detector, the slit width should be smaller than the source period; i.e., $P_s > s_w$.

To verify that we are indeed in a far-field regime, we consider the Fraunhofer distance when the coherence length is used as the source dimension:

$$d_F = 2\frac{\ell_c^2}{\lambda} = 2\lambda\left(\frac{L_1}{s_w}\right)^2. \tag{4}$$

We consider the coherence length because it is always equal to or greater than the grating period in the setup. To satisfy the far-field regime, L_2 should be greater than the Fraunhofer distance:

$$\frac{d_F}{L_2} \approx \frac{\lambda L}{s_w^2} \ll 1. \tag{5}$$

Given the experimental parameters of the monochromatic beamline $d_F/L_2 \approx 0.04$, polychromatic beamline $d_F/L_2 \approx 0.02$ for $\lambda = 0.5$ nm, and the beamline at the pulsed source $d_F/L_2 \approx 0.08$ for $\lambda = 0.35$ nm. The other two conditions for far-field regime are

$$L_2 \gg \lambda, \quad L_2 \gg s_w. \tag{6}$$

In our cases they are the least strict conditions.

If we consider equal period $P_{G_1} = P_{G_2} \equiv P_g$, $\pi/2$-phase gratings, with 50% comb fraction, then the maximum contrast is optimized for the condition $\delta_1(\lambda) = \delta_2(\lambda) = 0.5$ [25], where

$$\delta_1(\lambda) = \frac{\lambda L_1 D}{L P_g^2}, \quad \delta_2(\lambda) = \frac{\lambda L_2 D}{L P_g^2}. \tag{7}$$

The closed-form expression of the contrast is given by Eq. 12 in [25] and is computed numerically.

To align the gratings, the setup is initially arranged with theoretically calculated optimal slit width and lengths L_1, D, and L_2. Then one of the gratings is rotated around the neutron propagation axis (z axis) until the fringe pattern is observed at the camera. The contrast with the monochromatic setup as a function of the first grating rotation around the z axis is shown in the top plot of Fig. 2.

The slit height s_h (slit length along the x-axis direction in Fig. 1) can be larger than the slit width s_w in order to increase neutron intensity, provided that the gratings are well aligned to be parallel to that direction. The angular range of appreciable contrast is inversely related to the slit height $P_g/(2L_1 s_h/L)$. The expected range of $\pm 0.007^\circ$ agrees with the range depicted on Fig. 2.

The intensity of the fringe pattern recorded by the camera can be fit by a cosine function

$$I = A + B\cos(fx + \phi). \tag{8}$$

where x is the pixel location on the camera. Thus, the mean A, the amplitude B, the frequency f, and the differential phase ϕ can be extracted from the fit. The *contrast*, or *fringe visibility*, is given by

$$\mathcal{C} = \frac{\max\{I\} - \min\{I\}}{\max\{I\} + \min\{I\}} = \frac{B}{A}. \tag{9}$$

Due to the generally low neutron flux with monochromatic beamlines, the slit widths are optimized for intensity vs contrast. The contrast as a function of the slit width for the bichromatic setup is shown in the bottom plot of Fig. 2. Variation of the contrast vs slit width could be described by the sinc function

$$\mathcal{C} = \mathcal{C}_0 \left| \mathrm{sinc}\left[\frac{\pi s}{P_s}\right] \right|, \tag{10}$$

where $\mathcal{C}_0$ is the maximum achievable contrast with a given setup. Thus, given a slit width of one-third of the source period, in our case 281 μm, would give an upper bound of 83% contrast. The fit in the bottom plot of Fig. 2 gives a source period of $P_s = 843 \pm 43$ μm, which is in good agreement with $P_s = 845$ μm obtained with Eq. (3), where $D = 10$ mm.

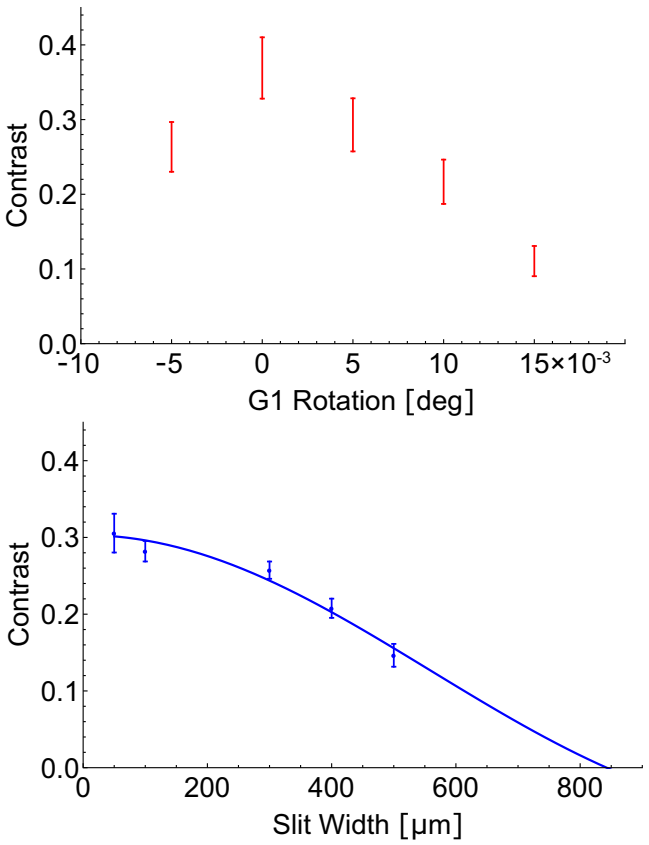

FIG. 2. Optimization data. (Top) The contrast is found by placing the gratings vertically and rotating one of them along the roll axis in very fine increments. The plot shows the contrast at the monochromatic beamline as a function of the first grating rotation around the neutron propagation axis. (Bottom) The dependence of the contrast at the bichromatic setup on the slit width s_w. The fit is given by applying Eq. (10) to the data and shows good agreement with the calculated source period P_s.

III. METHODS

The experiment was performed in four different configurations. The bichromatic and monochromatic beam configurations were performed at the NG7 NIOFa beamline [27] at the National Institute of Standards and Technology Center for Neutron Research (NCNR) with $L_1 = 1.73$ m and $L = 3.52$ m for bichromatic beam and $L_1 = 1.20$ m and $L = 2.99$ m for monochromatic beam. The neutron camera used in this setup has an active area of 25 mm diameter, with scintillator NE426 [ZnS(Ag) type with ^{6}Li as the neutron converter material] and a spatial resolution of $\sim$100 μm, and virtually no dark current noise [28]. Images were collected in 300-s-long exposures. The neutron quantum efficiency of the camera is 18% for $\lambda = 0.22$ nm and about 50% for $\lambda = 0.44$ nm. The neutron beam is extracted from a cold neutron guide by a pyrolytic graphite (PG) monochromator with $\lambda = 0.44$ nm and $\lambda = 0.22$ nm components with an approximate ratio of 3.2:1 in intensity. To change from bichromatic to monochromatic configuration, i.e., filter out the $\lambda = 0.22$ nm component, a liquid-nitrogen-cooled Be filter with nearly 100% filter efficiency [27] was installed downstream of the interferometer entrance slit. The slit width was set to 200 μm and slit height to 2.5 cm.

The polychromatic beam configuration was performed at the NG6 Cold Neutron Imaging (CNI) facility [29] at the NCNR. The CNI is located on the NG6 end station and has neutron spectrum approximately given by a Maxwell-Boltzmann distribution with $T_c = 40$ K or $\lambda_c = 0.5$ nm. The slit-to-detector length is $L = 8.8$ m and slit to G_1 distance is $L_1 = 4.65$ m. The slit width was set to 500 μm and slit height to 1.5 cm.

The imaging detector was an Andor sCMOS NEO camera viewing a 150-μm-thick LiF:ZnS scintillator with a Nikon 85-mm lens with a PK12 extension tube for a reproduction ratio of about 3.7, yielding a spatial resolution of $\eta = 150$ μm [30]. To reduce noise in the sCMOS system, the median of three images was used for analysis.

The fourth configuration used a pulsed neutron beam produced at the Energy-Resolved Neutron Imaging System (RADEN) [31], located at beam line BL22 of the Japan Proton Accelerator Research Complex (J-PARC) Materials and Life Science Experimental Facility (MLF). The wavelength range that was used was from 0.05 to 0.35 nm. The slit-to-detector length is $L = 8.6$ m and slit-to-G_1 distance is $L_1 = 4.24$ m. The slit width was set to 200 μm and slit height to 4 cm. The neutron imaging system employed a micropixel chamber (μPIC), a type of micropattern gaseous detector with a two-dimensional strip readout, coupled with an all-digital, high-speed field-programmable gate array (FPGA)-based data-acquisition system [32]. This event-type detector records the time of arrival of each neutron event relative to the pulse start time for precise measurement of neutron energy, and it has a spatial resolution of 280 μm (FWHM). The readout of the μPIC detector introduces a fixed-pattern noise structure which is completely removed by normalizing to empty beam measurements. Thus, the visibility measurements are from open-beam normalized images of the moiré pattern. The average number of detected neutron events was about 80 per 160-μm pixel with a 4-h integration time.

IV. RESULTS AND DISCUSSION

By observing the interference fringes with and without a sample that has been placed either upstream or downstream of the gratings, we can extract the conventional beam attenuation, dark-field contrast, and differential phase contrast. By varying the grating spacing D, this interferometer may also be employed to measure small-angle scattering of microstructures in the range of nm to several μm [33].

Figures 3(a)–3(d) show examples of typical images of the interference pattern obtained in optimized configurations for different beamlines: (a) bichromatic beam with $\lambda_1 = 0.22$ nm and $\lambda_2 = 0.44$ nm (b) same beamline as (a) but with a Be filter to completely eliminate the $\lambda_1 = 0.22$-nm-component (c) polychromatic neutron beam with peak wavelength $\lambda_c = 0.5$ nm and (d) a pulsed source for $\lambda = 0.25$ nm. In Fig. 3(a) the middle dark region corresponds to the collimator which was placed at the front in the setup and not the grating pattern. As the Be filter adds divergence to the beam, it can be seen that the dark middle region gets washed out in Fig. 3(b). The box on each image represents a region of integration along the vertical axis and the integral curve is shown under each image.

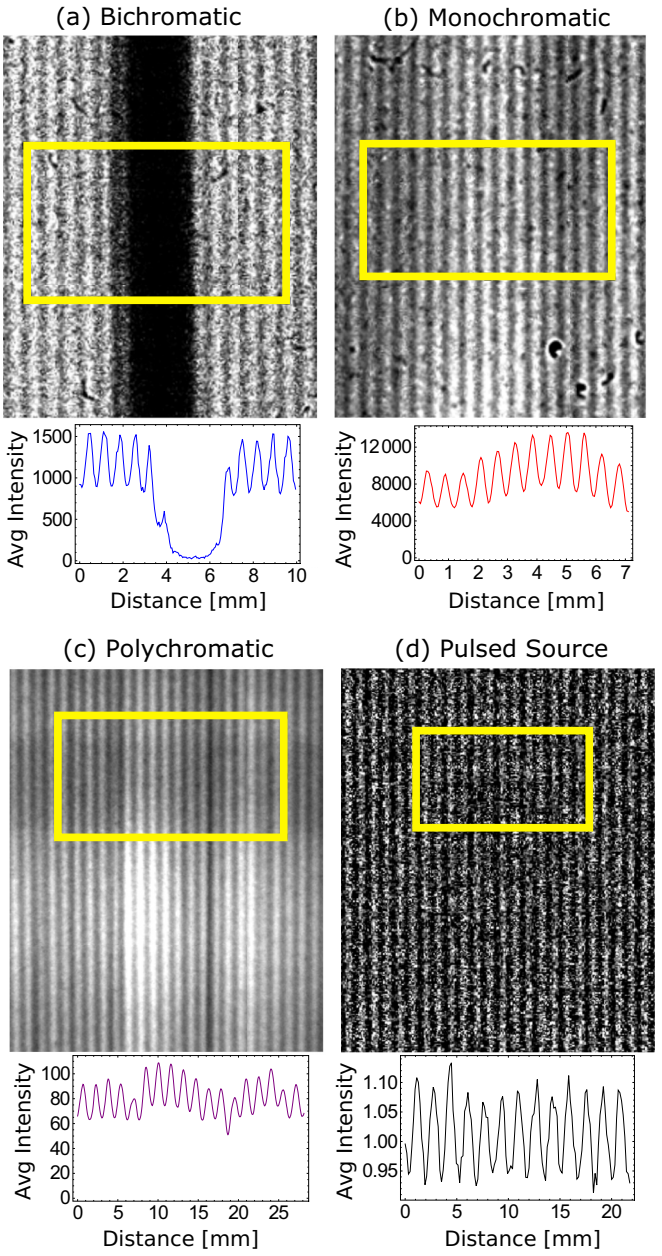

FIG. 3. Typical far-field images obtained with (a) 300-s exposure time with the bichromatic neutron beam, (b) 10000-s exposure time with the monochromatic neutron beam, and (c) median filter applied on three images with 2-s exposure time with the polychromatic neutron beam; (d) normalized image from the J-PARC pulsed source. The integrated intensities of the regions specified by the yellow rectangle show the observed fringe pattern at the camera. The dark region in the middle of the bichromatic image is due to the collimator in that particular setup and not due to the gratings.

Such integral curves were used to fit with Eq. [8] to extract phase and frequency and compute the contrast via Eq. [9].

The top plot in Fig. 4 shows contrast (fringe visibility) change versus grating separation, D. The data obtained at the National Institute of Standards and Technology (NIST) for the monochromatic, bichromatic and polychromatic beamlines are plotted on the same figure for comparison. The theoretically calculated contrast curves for the three conditions are also

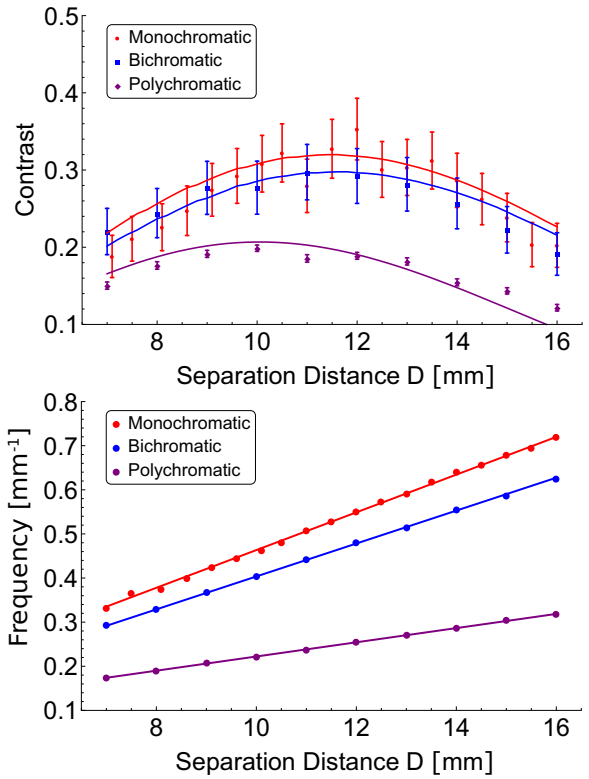

FIG. 4. (Top) The contrast as a function of the separation distance between the gratings for the monochromatic, bichromatic, and polychromatic neutron beams. The fits are given by Eq. 12 in [25], and the contrast for the monochromatic, bichromatic, and polychromatic beamlines is optimized at $D = 12$, 12, and 10 mm, respectively, agreeing well with theoretical predictions [25]. (Bottom) The frequency of the oscillation fringes varies linearly as a function of the distance between the gratings. The linear fit is according to $(D - D_0)/(L \times P_g)$, which for the monochromatic setup gives $D_0 = -0.75$ mm and $L = 3.04$ m, the bichromatic setup gives $D_0 = -0.8$ mm and $L = 3.51$ m, and polychromatic setup gives $D_0 = -3.8$ mm and $L = 8.36$ m. The exposure time was 2 s.

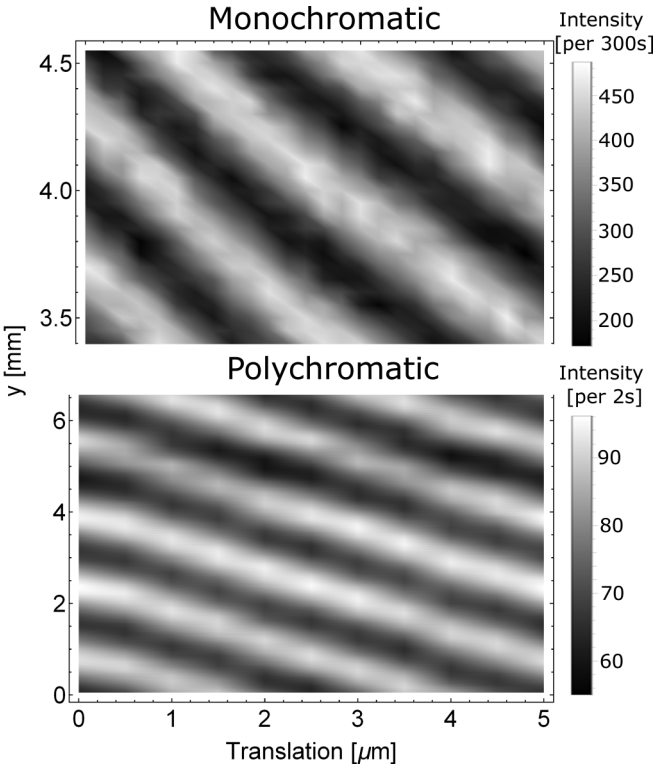

FIG. 5. Linear phase stepping is achieved with parallel translation of the first grating G_1 by increments smaller than the period of the gratings. (Top) Data from the monochromatic beamline. (Bottom) Data from the polychromatic beamline. In both cases linear dependence between the phase and grating translations is observed, while the contrast is preserved. Data were collected for the translation range of 0 to 5 μm, in increments of 0.2 μm (0.5 μm) for the monochromatic (polychromatic) plot.

plotted, which were based on estimates of 0.27π phase-shift gratings at 0.44 nm wavelength for the mono- and bichromatic setups and 0.2π phase shift at 0.5 nm wavelength for the polychromatic setup. The maximum contrast for the monochromatic, bichromatic, and polychromatic beamlines are achieved at $D = 12$, 12, and 10 mm, respectively, agreeing well with theoretical predictions [25]. Theoretical estimates indicate that there is room for improvement of contrast by improving grating profile and detector resolution. The bottom plot in Fig. 4 shows the linear dependence of the fringe frequency at the camera on the grating separation. As the distance between the gratings is increased, the period of the fringes at the camera is decreased. The linear fit is according to $(D - D_0)/(L \times P_g)$, which for the monochromatic setup gives $D_0 = -0.75$ mm and $L = 3.04$ m, the bichromatic setup gives $D_0 = -0.8$ mm and $L = 3.51$ m, and polychromatic setup gives $D_0 = -3.8$ mm and $L = 8.36$ m.

To implement phase stepping of the fringe pattern at the camera, one grating needs to be translated in plane in the perpendicular direction to the grating lines (along the y axis in Fig. 1 or along the grating vector). The translation step size needs to be smaller than the grating period. The top plot in Fig. 5 shows the two-dimensional plot of phase stepping for the monochromatic beamline setup; and the bottom plot in Fig. 5 shows the phase stepping for the polychromatic beamline setup. In both cases linear dependence between the phase and grating translation is observed, while the contrast is preserved.

Similar aligning procedures and measurements were performed at J-PARC spallation pulsed source. Figure 6 shows the contrast as a function of the wavelength for various grating separations. Due to the nature of the pulse source, we were able to extract contrast as a function of wavelength. Note that at the time of the experiments J-PARC was running at 200 KW as opposed to 1 MW due to technical problems. This lowered the neutron flux to 1/5 of the standard flux and the low intensity proved to be a significant challenge in terms of optimizing the setup for each independent wavelength.

The beam attenuation, decoherence, and phase-gradient images shown in Figs. 7(b)–7(d) are of an aluminum sample shown in Fig. 7(a). The approximate imaged area is depicted by the rectangular box. The images in Fig. 7(b)–7(d) were obtained by the Fourier transform method described in [34].

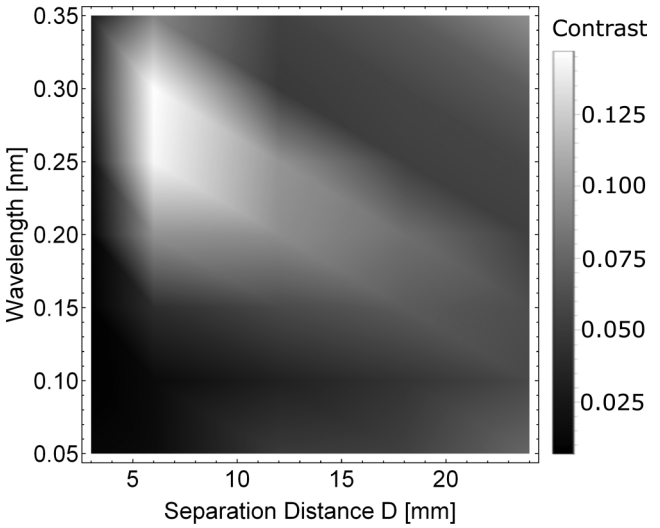

FIG. 6. Grayscale representation of the contrast (fringe visibility) dependence on neutron wavelength and gratings separation distance, D. Contrast data obtained with a pulsed neutron beam from a spallation source at J-PARC. Data were collected for the wavelength range of 0.05 to 0.35 nm, in increments of 0.05 nm, and for separation distance values of 3, 6, 12, 18, and 24 mm.

At the described polychromatic beamline at NIST three images with 20-s exposure time were taken at each step in the phase-stepping method [35]. A median filter was then applied to every set of three images. The phase step size was 0.24 μm, ranging from 0 to 2.4 μm of the G_2 transverse translation. The G_1-G_2 grating separation was $D = 11.5$ mm.

Figure 7(b) shows the conventional attenuation-contrast radiography of the sample, where white color represents full transmission (no attenuation). The shape and features of the sample are well defined in the image. Figure 7(c) shows the decoherence of the fringe contrast due to the sample, $-\ln(\mathcal{C}_{\text{sample}}/\mathcal{C}_{\text{empty}})$, where the white color represents loss of contrast and the black color represent no contrast reduction. As expected, the areas which caused the largest attenuation also caused the largest loss of contrast, likely due to small angle scattering from alloying. Figure 7(d) shows the phase shift in the moiré pattern at the detector due to the sample. The white and black patterns represent highest phase gradient that the neutrons acquire when passing through the sample.

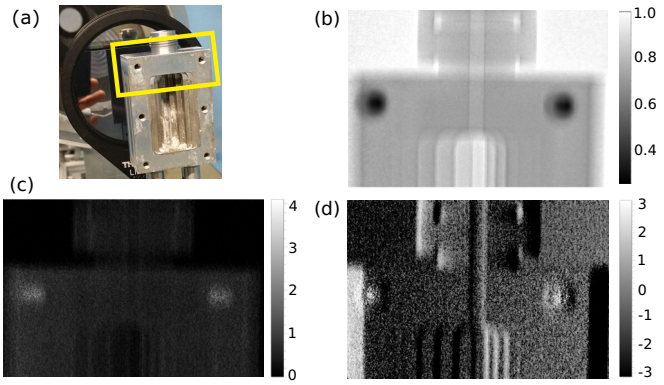

FIG. 7. Phase-contrast imaging with a polychromatic beam. (a) The aluminum sample in front of the G_1 grating. The yellow box roughly outlines what is being imaged. The sample has a step profile in the middle region and threaded screw holes in the corners. (b) Neutron attenuation image due to absorption and scattering. The grayscale bar represents transmission through the sample. (c) Spatial variation of the contrast attenuation due to the sample, $-\ln(\mathcal{C}_{\text{sample}}/\mathcal{C}_{\text{empty}})$. In this case white represents a loss in contrast, and black represents no loss in contrast. (d) Phase shift in the moiré pattern at the detector due to the sample. The grayscale bar represents radians. Here, the white and black patterns represent the highest phase gradient that the neutrons acquire when passing through the sample.

V. CONCLUSION

For the first time we have demonstrated a functioning two-phase-grating-based, moiré-effect neutron interferometer. The design has a broad wavelength acceptance and requires nonrigorous alignment. The interferometer operates in the far-field regime and can potentially circumvent many limitations of the single crystal and grating-based Mach-Zehnder-type interferometers and the near-field Talbot-Lau-type interferometers that are in operation today. Mach-Zehnder-type interferometers may provide the most precise and sensitive mode of measurements, but a successful implementation requires highly collimated and low-energy neutron beams. On the other hand, a near-field Talbot-Lau interferometer requires absorption analyzer gratings which curtail flux and interference fringe contrast. These constraints can be significant in a variety of applications.

The performance of our demonstration interferometer was limited primarily by grating imperfections and detector resolution. However, the design is simple and robust. We expect that the next generation of interferometers based on the far-field design will open new opportunities in high-precision phase-based measurements in materials science, condensed-matter physics, and bioscience research. In particular, because of the moiré fringe exploitation in this type of interferometers, the uses may be highly suitable for the studies of biological membranes, polymer thin films, and materials structure. Also, the modest cost and the simplicity of assembly and operation will allow this type of interferometer to have wide acceptance in small to modest research reactor facilities worldwide.

ACKNOWLEDGMENTS

This work was supported by the U.S. Department of Commerce, the NIST Radiation Physics Division, the director's office of NIST, the NIST Center for Neutron Research, and the National Institute of Standards and Technology (NIST) Quantum Information Program. The research results communicated here would not be possible without the significant contributions of the Canada First Research Excellence Fund (CFREF), the Canadian Excellence Research Chairs (CERC) program (215284), the Natural Sciences and Engineering Research Council of Canada (NSERC) Discovery program, and the Collaborative Research and Training Experience (CREATE) program (414061). D.A.P. is grateful for discussions with Michael Slutsky.

[1] J. Chadwick, Nature (London) **129**, 312 (1932).

[2] H. Maier-Leibnitz and T. Springer, Z. Physik **167**, 386 (1962).

[3] H. Rauch and S. A. Werner, *Neutron Interferometry: Lessons in Experimental Quantum Mechanics, Wave-Particle Duality, and Entanglement*, 2nd ed. (Oxford University Press, Oxford, UK, 2015), Vol. 12.

[4] C. W. Clark, R. Barankov, M. G. Huber, M. Arif, D. G. Cory, and D. A. Pushin, Nature (London) **525**, 504 (2015).

[5] K. Li, M. Arif, D. Cory, R. Haun, B. Heacock, M. Huber, J. Nsofini, D. Pushin, P. Saggu, D. Sarenac *et al.*, Phys. Rev. D **93**, 062001 (2016).

[6] D. A. Pushin, M. Arif, and D. G. Cory, Phys. Rev. A **79**, 053635 (2009).

[7] D. Sarenac, M. G. Huber, B. Heacock, M. Arif, C. W. Clark, D. G. Cory, C. B. Shahi, and D. A. Pushin, Opt. Express **24**, 22528 (2016).

[8] J. Klepp, S. Sponar, and Y. Hasegawa, Prog. Theor. Exp. Phys. **2014**, 82A01 (2014).

[9] T. Denkmayr, H. Geppert, S. Sponar, H. Lemmel, A. Matzkin, J. Tollaksen, and Y. Hasegawa, Nat. Commun. **5**, 4492 (2014).

[10] M. Arif, D. E. Brown, G. L. Greene, R. Clothier, and K. Littrell, Proc. SPIE **2264**, 20 (1994).

[11] P. Saggu, T. Mineeva, M. Arif, D. Cory, R. Haun, B. Heacock, M. Huber, K. Li, J. Nsofini, D. Sarenac *et al.*, Rev. Sci. Instrum. **87**, 123507 (2016).

[12] A. I. Ioffe, V. S. Zabiyakin, and G. M. Drabkin, Phys. Lett. **111**, 373 (1985).

[13] M. Gruber, K. Eder, A. Zeilinger, R. Gähler, and W. Mampe, Phys. Lett. A **140**, 363 (1989).

[14] G. van der Zouw, M. Weber, J. Felber, R. Gähler, P. Geltenbort, and A. Zeilinger, Nucl. Instrum. Methods Phys. Res., Sect. A **440**, 568 (2000).

[15] U. Schellhorn, R. A. Rupp, S. Breer, and R. P. May, Phys. B Condens. Matter **234–236**, 1068 (1997).

[16] J. Klepp, C. Pruner, Y. Tomita, C. Plonka-Spehr, P. Geltenbort, S. Ivanov, G. Manzin, K. H. Andersen, J. Kohlbrecher, M. A. Ellabban, and M. Fally, Phys. Rev. A **84**, 013621 (2011).

[17] J. F. Clauser and S. Li, Phys. Rev. A **49**, R2213 (1994).

[18] F. Pfeiffer, C. Grünzweig, O. Bunk, G. Frei, E. Lehmann, and C. David, Phys. Rev. Lett. **96**, 215505 (2006).

[19] H. Talbot, Philos. Mag. Ser. 3 **9**, 401 (1836).

[20] A. D. Cronin and B. McMorran, Phys. Rev. A **74**, 061602 (2006).

[21] C. David, B. Nöhammer, H. Solak, and E. Ziegler, Appl. Phys. Lett. **81**, 3287 (2002).

[22] A. D. Cronin, J. Schmiedmayer, and D. E. Pritchard, Rev. Mod. Phys. **81**, 1051 (2009).

[23] M. S. Chapman, C. R. Ekstrom, T. D. Hammond, J. Schmiedmayer, B. E. Tannian, S. Wehinger, and D. E. Pritchard, Phys. Rev. A **51**, R14 (1995).

[24] E. Lau, Ann. Phys. **437**, 417 (1948).

[25] H. Miao, A. Panna, A. A. Gomella, E. E. Bennett, S. Znati, L. Chen, and H. Wen, Nat. Phys. **12**, 830 (2016).

[26] R. E. Williams and J. M. Rowe, Physica B **311**, 117 (2002).

[27] C. Shahi, M. Arif, D. Cory, T. Mineeva, J. Nsofini, D. Sarenac, C. Williams, M. Huber, and D. Pushin, Nucl. Instrum. Methods Phys. Res., Sect. A **813**, 111 (2016).

[28] M. Dietze, J. Felber, K. Raum, and C. Rausch, Nucl. Instrum. Methods Phys. Res., Sect. A **377**, 320 (1996).

[29] D. Hussey, C. Brocker, J. Cook, D. Jacobson, T. Gentile, W. Chen, E. Baltic, D. Baxter, J. Doskow, and M. Arif, Phys. Proc. **69**, 48 (2015).

[30] Certain trade names and company products are mentioned in the text or identified in an illustration in order to adequately specify the experimental procedure and equipment used. In no case does such identification imply recommendation or endorsement by the National Institute of Standards and Technology; nor does it imply that the products are necessarily the best available for the purpose.

[31] T. Shinohara and T. Kai, Neutron News **26**, 11 (2015).

[32] J. Parker, K. Hattori, H. Fujioka, M. Harada, S. Iwaki, S. Kabuki, Y. Kishimoto, H. Kubo, S. Kurosawa, K. Miuchi *et al.*, Nucl. Instrum. Methods Phys. Res., Sect. A **697**, 23 (2013).

[33] D. S. Hussey, H. Miao, G. Yuan, D. Pushin, D. Sarenac, M. G. Huber, D. L. Jacobson, J. M. LaManna, and H. Wen, arXiv:1606.03054.

[34] H. Wen, E. E. Bennett, M. M. Hegedus, and S. C. Carroll, Medical Imaging, IEEE Trans. Med. Imaging **27**, 997 (2008).

[35] J. H. Bruning, D. R. Herriott, J. Gallagher, D. Rosenfeld, A. White, and D. Brangaccio, Appl. Opt. **13**, 2693 (1974).